ANNALS OF GEOPHYSICS, 66, 6, SE 646, 2023; doi:10.4401/ag-8992
OPEN ACCESS

Multi-parametric study of seismogenic anomalies during the 2021 Crete earthquake (M = 6.0)

Sudipta Sasmal[*,1], Swati Chowdhury[2,8], Subrata Kundu[2], Soujan Ghosh[3], Dimitrios Z. Politis[4], Stelios M. Potirakis[4,5], Masashi Hayakawa[6,7]

(1) Institute of Astronomy Space and Earth Science, Kolkata, India
(2) Indian Centre for Space Physics, Kolkata, India
(3) National Atmospheric Research Laboratory, Gedanki, India
(4) Department of Electrical and Electronics Engineering, University of West Attica, Aigaleo-Athens, Greece
(5) Institute for Astronomy, Astrophysics, Space Applications and Remote Sensing, National Observatory of Athens, Penteli-Athens, Greece
(6) Hayakawa Institute of Seismo Electromagnetics, Co. Ltd, Chofu-Tokyo, Japan
(7) The University of Electro-Communications, Advanced & Wireless Communication Research Center, Chofu, Tokyo, Japan
(8) Space Physics Laboratory, VSSC, ISRO, Thiruvananthapuram - 695022, Kerala, India

Article history: received June 1, 2023; accepted December 28, 2023

Abstract

It is well established that pre- and co-seismic irregularities in the earth's atmosphere highly depend on a set of parameters. According to the Lithosphere-Atmosphere-Ionosphere Coupling (LAIC) mechanism, these parameters are associated with various channels (thermal, chemical, acoustic, electromagnetic, etc.) through which an earthquake (EQ) preparation process can have its anomalous phenomena. In this research, we perform a multi-parametric observation using various channels during a strong EQ (M = 6.0) on September 27, 2021, on Crete Island in Greece. We investigate the acoustic and electromagnetic channel using ground and satellite-based observation. We present the Atmospheric Gravity Wave (AGW) in the acoustic channel using the temperature profile computed from the SABER/TIMED instrument. In the electromagnetic channel, ionospheric Total Electron Content (TEC) is recorded by the GNSS-IGS station DYNG in Greece. This TEC information is also used in the acoustic channel anomaly by computing the wave-like structures in the small-scale fluctuation of the TEC profile. We compute energetic (30 to 100 keV) electron precipitation in the inner radiation belt from the NOAA satellite. We also investigate the outcomes of the SWARM satellite to compute the magnetic field and electron density profile. All the parameters show significant seismogenic anomalies (mostly enhancement) before the EQ. To understand each parameter's temporal and spatial sensitivity, we present a comparison using the anomalies in each parameter.

Keywords: Pre-seismic processes; Lithosphere-Atmosphere-Ionosphere Coupling (LAIC); Atmospheric gravity waves (AGWs); Total electron content (TEC); Radiation belt particle precipitation; Atmospheric electricity

1. Introduction

The overall physical processes involved in seismic events' generation mechanism are highly complex. A combination of geophysical and geochemical methods leading to an earthquake (EQ) is not only a conversion of strain energy to mechanical energy, but also it has a lot of pre-, intermediate, and post-EQ phenomena that originate this complexity [Shalimov, 1992; Pulinets, 2010; Hawakawa et al., 1996; Clilverd et al., 1999; Liu et al., 2011]. From the 1960s onwards to the present day, seismic hazard mechanisms turned into a new direction where the EQs are thought to be no longer an isolated phenomenon associated with the Earth's surface and underground it but having a connection with its atmosphere and outer space [Pulinets and Boyarchuk, 2004]. This connection can be attributed with majorly three to four channels viz. (a) chemical, (b) thermal, (c) acoustic, and (d) electromagnetic (EM). They can connect the pre- and co-seismic phenomena through the various layers of the earth's atmosphere, known as the Lithosphere-Atmosphere-Ionosphere-Coupling (LAIC) mechanism [Pulinets and Ouzounov, 2011]. LAIC exhibits a few crucial characteristics of seismic hazards and its preparation processes. It has been found that the pre-EQ processes following the different channels of LAIC are primarily non-linear, inhomogeneous, and anisotropic. As the physical mechanism of the individual channels during or prior to the EQs are different, this LAIC hypothesis requires multiple parameters at different domains to justify the response of that channel. So, to understand the pre-seismic impression at different channels, a multiparametric approach is necessary for this study [Sasmal et al., 2021].

The exciting theory of seismo-atmospheric coupling has been widely applied using individual parameters in different channels for various moderate to strong EQs. Starting from 1964, consistent research on the pre-seismic anomalies was comprehensively reported by many scientists mostly using the geo-chemical process that initiates the radio-active ionization that originates a modulation in EM radio wave propagation characteristics [Rozhnoi et al., 2013; Hayakawa, 2007]. The modulation of sub-ionospheric Very Low Frequency (VLF) radio waves and the emission of Ultra-Low-Frequency (ULF) radio waves show a significant anomaly in their characteristics before the occurrence of seismic events [Hayakawa, 1996(a); Hayakawa 1996(b); Molchanov et al., 1995; Potirakis et al., 2016]. After the LAIC hypothesis was established [Pulinets et al., 2011], anomalies in multiple parameters were considered to investigate the seismogenic effects in different channels as prescribed in this theory. The thermal channel and the anomalies associated with this are found to be a significant source of increasing the earth's radiation budget before EQs [Gorny et al., 1998; Chakraborty et al., 2017; Ghosh et al., 2022(a); Liu et al., 2000]. The thermal anomalies can be primarily attributed to parameters like surface and air temperature, surface latent heat flux (SLHF), outgoing longwave radiation (OLR), and relative humidity (RH). A substantial change (mostly increase) in such parameters has been presented by satellite observation and is found to be highly pre-seismic [Ghosh et al., 2022(b)].

It is found that the effect of these thermal irregularities can create a convection mechanism in the lower and middle atmosphere that includes buoyancy and air parcel movements, generating the concept of an acoustic channel of LAIC. The Atmospheric Gravity Waves (AGWs) are the main parameter in this channel that is crucial for transporting the energy from the lower atmosphere to the stratosphere and mesosphere. It is proposed that during the strain energy accumulation process of EQs, temperature modulation, thermal conductivity, and pressure can generate wave-like structures in the frequency bandwidth of AGWs. Ground and space-based techniques can detect such intensified wave energy. This primarily includes radars, GPS, satellites, and Low-frequency radio receivers [Thurairajah et al., 2014; Piersanti et al., 2020; Biswas et al., 2020; Chakraborty et al., 2017; Korepanov et al., 2009; Politis et al., 2022]. The satellite-based detection procedure involves the stratospheric temperature variation to compute the potential energy of the intensified AGWs, which is highly useful for detecting seismogenic effects in the acoustic channel.

The EM channel of LAIC involves a wide range of parameters, some of which are interconnected in nature. It has been found that the temporal variation of the different anomalous parameters in the EM channel shows an anisotropy and inhomogeneity even though for the same EQ. Thus, all the parameters often do not show simultaneous effects during the pre-seismic period, even for the same EQ. This channel also includes a wide range of altitudes from beneath the earth's surface to magnetospheric heights. The anomalous emission and depression in Ultra Low Frequency (ULF) signal near the EQ epicenter can be treated as direct evidence of pre-seismic impression [Schekotov et al., 2006; Hayakawa et al., 2019, 2023]. This emission can be directly linked with magnetospheric variabilities by the concept of energetic particle burst in the radiation belt [Anagnostopoulos et al., 2012; Fidani et al., 2008; Fidani et al., 2021; Fidani et al., 2022; Chowdhury et al., 2022; Battiston et al., 2013]. Thus, this particle burst can be treated as significant indirect evidence of the seismogenic anomalies in the upper atmosphere. In the upper atmosphere, ionospheric variabilities during and before EQs can be well estimated through the sub-ionospheric VLF radio-sounding techniques [Chakrabarti et al., 2005; Chakrabarti et al., 2007; Sasmal et al., 2009; Chakrabarti et al., 2010; Chakraborty et al., 2017; Biswas et al., 2022; Biswas et al., 2023; Ghosh et al., 2019; Pal et al., 2017; Maurya et al., 2016; Nina et al., 2021; Politis et al., 2021; Potirakis et al., 2018a; Ray et al., 2010; Ray et al., 2011; Ray et al., 2012; Sasmal et al., 2010; Sasmal et al., 2014; Yoshida et al., 2008; Rozhnoi et al., 2014a; Rozhnoi et al., 2013; Popov et al., 2004]. Another important parameter is the F-layer's critical frequency, which shows significant anomalies before the EQs [Ghosh et al., 2017]. The ionospheric Total Electron Content (TEC), as computed by Global Navigation Satellites System (GNSS), is one of the most promising ground-based tools for the detection of possible seismo-electromagnetic effects. The diurnal modulation is a useful study when the TEC value usually increases before strong EQs [Agrner et al., 2008; Liu et al., 2001; Liu et al., 2004]. TEC profiles can also detect small and medium-scale traveling ionospheric disturbances (TIDs) by extracting the small-scale fluctuations in the differential TEC profiles (dTEC). Statistical and case-wise studies show that the atmospheric magnetic field and the electron density profiles show significant anomalies before strong EQs as observed from the Swarm satellites missions [Balasis et al., 2007; De Santis et al., 2015, He et al., 2022]. Additionally, more essential parameters like surface deformation data from GPS observation [Yang et al., 2020], aerosol anomaly [Ghosh et al., 2023], etc., are also found to be significant for detecting seismogenic anomalies. Recently Chen et al. [2022] and Hayakawa et al. [2023] published two detailed reviews on the seismo-electromagnetic pre-EQ phenomena.

In Sasmal et al. [2021], an extensive review of the used parameters has been presented where the past works and the utilization of each parameter have been reported elaborately. The pre-seismic response of acoustic and EM channels is reported during the 2021 Samos (Greece) EQ ($M = 6.9$) by using parameters like AGW, TEC, radiation belt electron precipitation, magnetic field, and electron density as observed from various ground and space-based studies. Politis et al. [2021] present a comprehensive analysis of VLF radio signal anomalies separately during the same EQ. Hayakawa et al. [2021, 2022], Chetia [2020], Marchetti et al. [2019], Ouzounov et al. [2021], Wu et al. [2023] and Zang et al. [2023] reported a similar extensive study for EQs in Japan, Italy, Nepal and China including more parameters like ULF/ELF emissions, VLF anomaly, air temperature, etc. that mostly corroborates the previous findings. In this manuscript, we continue this study with a similar approach for another strong EQ that took place on Crete Island in Greece on September 27, 2021, having the magnitude of $M = 6$. One of the prime objectives of this study is to check and validate the temporal and spatial variations of the above-mentioned parameters with the previously well-established results for a different condition and higher EQ magnitude ($M = 6.7$) and to find any diversification from the previously reported results. This manuscript deals with AGW excitation in the acoustic channel and GNSS-TEC, radiation belt electron precipitation, and electron density variations detected by Swarm satellite in the EM channel of LAIC. The plan of the paper is as follows. The following section gives the methodology for extracting the various parameters. In Section 3, we present our results. Finally, in sections 4 and 5, we discuss the results and draw conclusions, respectively.

2. Date and Methodology

The EQ we have chosen took place on 27 September 2021 at 06:17;21 UTC with magnitude $M = 6.0$ with a depth of 6 kilometers in the central part of the island of Crete, Greece, at ~20 km to the south of the capital city of Crete, Heraklion. Figure 1 shows the position of the EQ epicenter marked with a red circle. The EQ preparation zone (EPZ) computed from the Dobrovolsky formula [Dobrovolsky, 1979] is ~380 kilometers and shown in Figure 1. Figure 1 also shows the position of the IGS station DYNG by yellow diamond.

2.1 Atmospheric Gravity Waves (AGWs) computation

In this work, we use the altitude profile of atmospheric temperature as recorded by Sounding of the Atmosphere utilizing Broadband Emission Radiometry (SABER) instrument installed on the Thermosphere Ionosphere Mesosphere Energetics and Dynamics (TIMED) satellite to identify the wave-like structures. The computation of the information of AGWs follows the conventional methods as prescribed by Remsberg et al. [2008] Fetzer et al. [1994], Kundu et al. [2022], Sasmal et al. [2021], and Biswas et al. [2020]. The SABER instrument of the TIMED satellite has an orbital height of 625 kilometers and a period of 1.7 hours, with an inclination of 74.1°. By using the wavelength range from 1.27 to 17 mm, SABER can record the atmospheric temperature from 20 to 100 kilometers. We follow

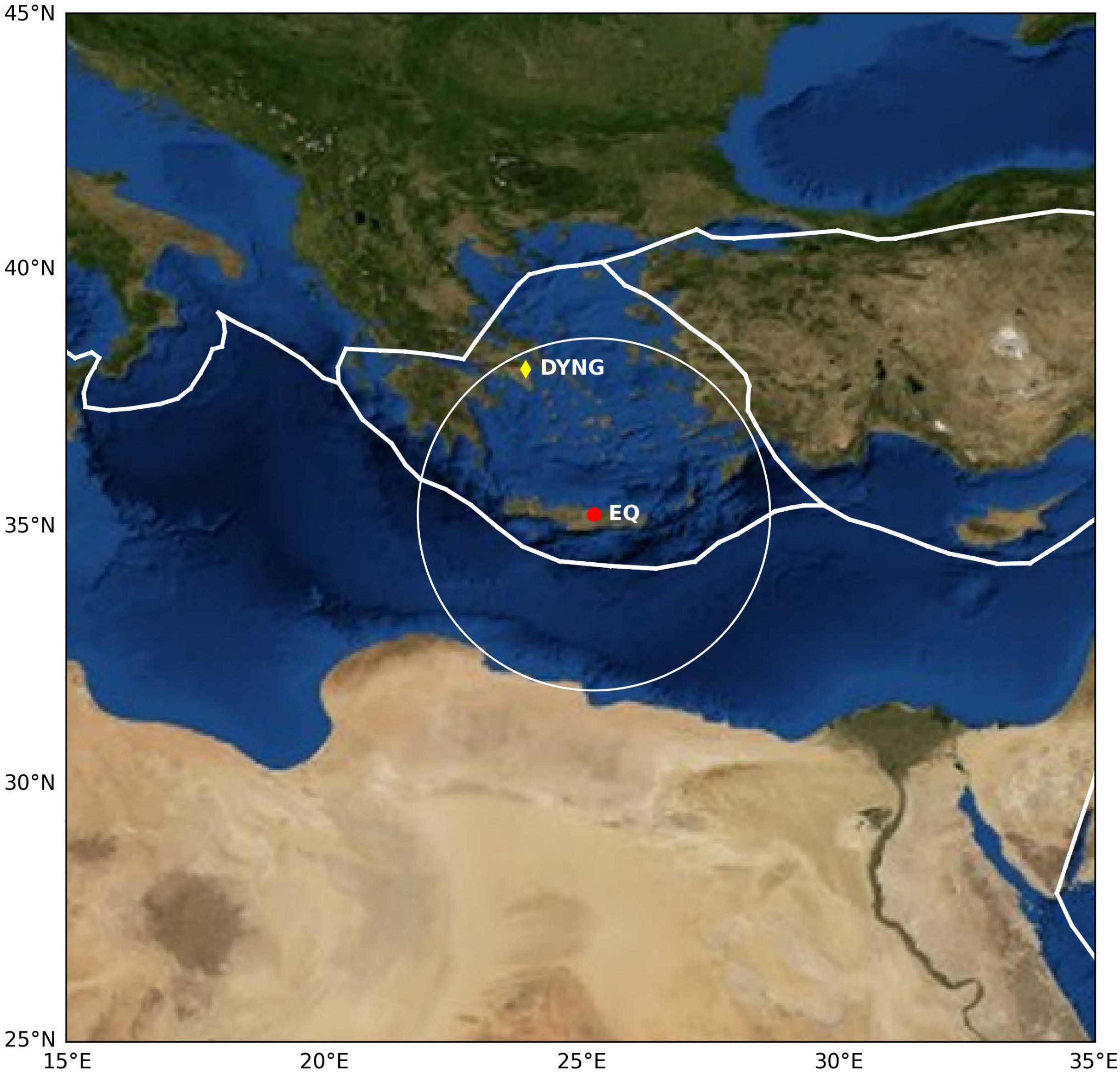

Figure 1. The location of the EQ epicenter (red circle), the IGS station (yellow diamond), and the Dobrovolsky area of the EQ preparation zone.

the previous methodologies done by Sasmal et al. [2021] and Kundu et al. [2021] where the altitude profile of the temperature (T) for a specific geographic region with a finite latitude/longitude range is extracted from SABER data archive (http://saber.gats-inc.com/). At first, we compute the logarithmic temperature profile and fit this with a third-degree polynomial. The residual values are computed from the difference between the original and fitted profile. A 4 km boxcar filter is added to the residual profile to eliminate all other waves with a wavelength shorter than 4 km. Combining the filtered residual values with the fitted values generates the final profile. By taking the antilogarithm of this profile, the least square fit of this profile is achieved. We compute the regular zonal mean temperature and other zonal wave components using these LSFs ranging from 1 to 5. We treat all the wave components having wave numbers 0 to 5 as the background temperature profile (T_0). The perturbation temperature profile (T_p) can be obtained by subtracting the original profile from the background profile. The potential energy (E_p) associated with AGW is computed by putting the values in the following equation:

$$E_p = \frac{1}{2}\left(\frac{g}{N}\right)^2 \left(\frac{T_p}{T_0}\right)^2. \quad \text{(i)}$$

Here g is the gravity acceleration and N is Brunt-Väisälä frequency described as,

$$N^2 = \frac{g}{T_0}\left(\frac{\partial T_0}{\partial z} + \frac{g}{c_p}\right). \tag{ii}$$

Here, z is the altitude, and c_p is the specific heat at constant pressure. After the computation of the E_p, a nine-dimensional matrix is generated having the components as latitude, longitude, date or day of the year in UT, altitude, original SABER temperature profile, reconstructed fitted temperature profile, perturbation temperature, Brunt-Väisälä frequency, and E_p. For the Crete EQ, we choose the spatial span of latitude and longitude ranges from 25° to 45° N and 15° to 25° E keeping the EQ epicenter as the center.

2.2 Computation of Total Electron Content (TEC)

We first focus on the ionospheric TEC variation to study the seismogenic impact in the EM channel of LAIC. To compute diurnal TEC profiles, we use the GPS-IGS station DYNG (38.078° N, 23.93° E) in Greece, which is close to the epicenter of the EQ.

To compute the TEC values from RINEX input, we follow the well-known software provided by Gopi Seemala [Seemala et al., 2011]. It is well established [Sasmal et al., 2021] that the vertical TEC ($VTEC$) can be expressed as,

$$VTEC = \frac{STEC - TEC_{cal}}{M(\alpha)}. \tag{iii}$$

Here, $STEC$ is the Slant TEC and $TEC_{cal} = (b_s + b_r + b_{RX})$, where b_s is the satellite bias, b_r is the receiver bias and b_{RX} is the receiver inter-channel bias. By using the methodology reported by Mannuchi et al. [1993] and Langley et al. [2002], we compute the $M(\alpha)$ as,

$$M(\alpha) = \frac{1}{Cos(\beta)} = \left(1 - \frac{R_e Cos(\alpha)}{R_e + h_{min}}\right)^{-0.5}. \tag{iv}$$

R_e is the earth's radius, h_{min} is the Ionospheric Pierce Point (IPP) at an altitude of 350 km, α is the zenith angle at the receiver side and β is the elevation angle at the IPP. The bias correction and the calibration of TEC are done by the methods reported in the previous methodology in Seemala and Valldares [2011]. We study the anomalous VTEC profile for a duration of $\pm$15 days around the EQ. We compute the median χ of the VTEC values for the past 15 days of the EQ and the corresponding interquartile range (IQR). Based on this computation, an upper bound (UB) and lower bound (LB) have been computed for a specific time (UT,) and that is given by,

$$UB = \chi + IQR,$$

$$LB = \chi - IQR.$$

As reported in Klotz and Johnson [1983], the estimated values of χ and IQR for VTEC in a normal distribution having the mean (μ) and standard deviation (σ) are μ and 1.34σ respectively. The VTEC is treated to be anomalous with a confidence level of 80% to 85%, when it crosses either the UB or LB. Thus, the condition for anomaly is treated as,

$$anomaly = VTEC \geq UB,$$

and,

$$anomaly = VTEC \leq LB.$$

2.3 Computation of AGW from GPS-TEC

Traveling Ionospheric Disturbances (TIDs) are small-scale fluctuations caused by acoustic/atmospheric GWs (gravity waves) that can be produced due to various seismic and meteorological events. These fluctuations can be recorded from various techniques. GPS signal can detect these TIDs during its propagation, which can significantly influence the TEC profiles even for a short distance. To extract these wave-like structures, a fitting method is useful that is commonly known as "Savitzky-Golay filtering" (sgolayfilt) [Savitzky et al., 1964, 1989]. In this method, the weighting coefficients for a smoothing operation can be attributed by a set of integers (C−n, C−(n1) 391 ..., Cn−1, Cn). These sets of integers act as weighting coefficients, follow a similar technique of fitting with a polynomial with more efficiency. Therefore, the Savitzky-Golay technique, provides the smoothed data points (xi) s with an excellent fitting tool using the following equation:

$$(x_i)_s = \frac{\sum_{i=-n}^{i=n} C_i x_{i+1}}{\sum_{i=-n}^{i=n} C_i}. \tag{v}$$

To get information on the small-scale fluctuations, the $VTEC$ ($dVTEC$) change is computed by subtracting the original profiles from the fitted profile ($VTEC_f$). We use the sgloayfilt with a 5 degree polynomial and a window size of 90 minutes. Therefore,

$$dVTEC = VTEC - VTEC_f.$$

We perform a wavelet analysis using the complex Morlet continuous wavelet transformation and generate the scalograms to identify the wave-like structures. The intensified wave-like structures with periods of AGWs can be examined inside the Cone of Influence (COI) [Sasmal et al., 2021].

2.4 Computation of Particle Bursts (PBs)

The LAIC hypothesis suggests that an EQ having large magnitude can directly interfere with the radiation belt energetic particle counts by the process of ULF wave emission through the EQ epicentre. To examine such effects, we use the electron channel information of the Medium Energy Proton Electron Detector (MEPED) onboard NOAA satellite. The satellite provides the raw and processed information of such particle counts. We choose the duration of our observation for a period of 31 days (September 12 to October 12, 2021). For the computation of particle bursts (PBs), we follow the methods prescribed in Fidani et al. [2010], Chakraborty et al. [2019], Sasmal et al. [2021] and Chowdhury et al. [2022]. Firstly, we calculate the daily averages of the count rates (CRs) and define the condition for which the CR can be treated as PBs instead of statistical fluctuations. For the computation of particle counts, we convert the original datasets into a secondary dataset on daily basis. Each dataset contains parameters like time in milliseconds, latitude in degree, longitude in degree, MEPED electron channel information (electron count rates), IGRF magnetic field (B), MEPED telescope pitch angle (α), and L values (McIlwain L-parameter). It is well known that the South Atlantic Anomaly (SAA) has significant influences on the CR values of the radiation belt particles CR values due to a sharp gradient of particle flux in the South Atlantic regions. We choose an acceptable condition of B to eliminate the effects of SAA as $B > 22.0$ μT. To eliminate a similar effect of the transition between in the inner and outer radiation belt, we choose $L > 2.2$. As all the above-mentioned datasets of the orbital parameters are provided every 8 seconds, we choose this base time for our study and we take 8 s averages of all the parameters. The energies for the electrons are a cumulative sum over three thresholds having values $E_1 = 30$ keV, $E_2 = 100$ keV and $E_3 = 300$ keV. For further analysis, from the difference of these energy thresholds, we defined new energy channels to detect the electrons in the energy ranges 30 – 100 keV, 100 – 300 keV ad > 300 keV. We make a three-dimensional matrix with L, α, and B values where the binning of L value ranges from 0.9 to 2.2 having a bin width of 0.1. The pitch angle range (0 to 180°) is divided into 12 steps of 15° each. The geomagnetic field B is divided into nine ranges as: 16.0-17.5 μT, 17.5-19.0 μT, 19.0-20.5 μT, 20.5-22.0 μT, 22.0-25.0 μT, 25.0-29.0 μT, 29.0-33.0 μT, 33.0-37.0 μT, and 37.0-41.0 μT. Out of the 9 intervals, we consider only those B intervals for which its value is greater than 22:0 μT. Thus, we give importance on only 5 B intervals. For accurate statistics, only those L, α, and B shells are taken, in which the satellite passed at least 20 times through the same cell. In the next stage, we choose a condition where the CRs can be treated as PBs. For the previous results, the 8 seconds average can be treated as a Poisson distribution. So, for CR with non-Poisson distribution with 99% probability, the CRs must have values greater than or cross the 4σ value and can be treated as PBs where σ is the standard deviation [Chakraborty et al., 2019; Sasmal et al., 2021; Chowdhury et al., 2022].

It is an absolute need to find out whether the PBs are probably due to sesimogenic or not. For this we use the methods prescribed by Aleksandrin et al. [2003], where a condition can segregate the PBs only EQ generated. The condition incorporates the difference between the EQ associated L-shell (L_{EQ}) and PBs associated L-shell (L_{PB}). We consider the L_{EQ} is a point above EQ epicentre. This altitude can be 300 km where EQ generated EM waves can interact with earth's magnetosphere [Molchanov et al, 1993]. We choose only the EQ- induced PBs for which the condition $|\Delta L| = |L_{EQ} - L_{PB}| \leq 0.1$ is satisfied.

2.5 Swarm Satellite Analysis

The Swarm satellite mission, comprised of three individual satellites named Alpha (SATA), Bravo (SATB), and Charlie (SATC), was launched into a near-polar orbit on 22 November 22, 2013 [Friis-Christensen et al., 2008; Olsen et al., 2013; Yufei et al., 2021; Marchetti et al., 2022]. The prime objectives of the mission are precise measurement and monitoring of the spatio-temporal geomagnetic field profiles of the Earth. This satellite consists of advanced magnetometers and other sensors that monitor the Earth's geomagnetic field, plasma dynamics, and the electric field in the upper atmosphere. The Langmuir Probes are used as plasma sensors for studying the seismo-ionospheric coupling mechanisms. Sasmal et al. [2021] performed an extensive discussion of the satellite's components and the extraction of the Swarm satellite's magnetic field plasma data structure. The different magnetic field components were presented by using the MASS algorithm [De Santis et al., 2015; De Santis et al., 2019; De Santis et al., 2019] and the electron density profiles was examined with NeLOG and NeSTAD algorithm [De Santis et al., 2019]. In this manuscript, we use a method called the rapid disturbance of the satellite observation data [Yufei et al., 2021]. These rapid disturbances of the satellite orbital data can be computed by a best fitting curve of the datasets that can be obtained by a cubic spline smooth method. This method involves the electron density profiles as gathered from the swarm satellite's database (https://swarm-diss.eo.esa.int). To quantify rapid disturbances, the percentage (P) of the disturbance relative to the fitting data is computed by the formula,

$$P = [(O - F)/F] * 100\%,$$

where O is the orbital data and F is the fitting data. For getting more reliable outcomes, the continuous disturbances that are greater than 3% are taken as one disturbance [He et al., 2022]. The mean latitude, longitude and time of the three continuous points are considered as the location and time of the anomaly. Also, as the time for the satellite to cross the EQ epicener is very short, if multiple disturbances take place during that time, they are still taken as one disturbance. The percentages disturbances, latitude, longitude and time, are taken to identify the seismogenic effects in the electron density profile. To eliminate any contamination due to geomagnetic activity, the geomagnetic indices need to be compared with all the disturbances to exclusively find out the anomaly likely due to seismic origin.

3. Results

Solar activities and geomagnetic conditions act as the most significant contaminating parameters during the investigation of any EM seismogenic anomalies, and it is required to eliminate such contamination from the observed outcomes. In Figure 2(a), we present the variation of Dst, Kp (3 hours average), ap (3 hours average) and

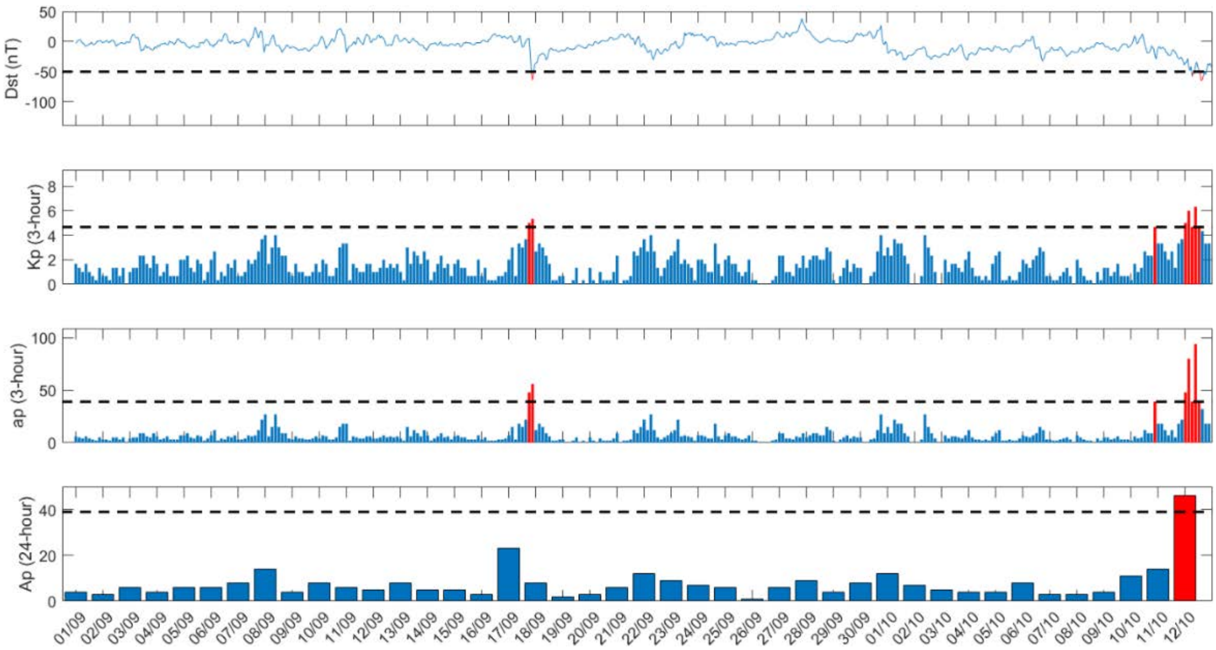

Figure 2a. Temporal variation of geomagnetic indices during the time period of 1 September 2021 - 12 October 2021 (from top to bottom panel): Dst, Kp, ap, and Ap. The red-colored histograms indicate values those exceed the corresponding thresholds marked by the horizontal black dashed line.

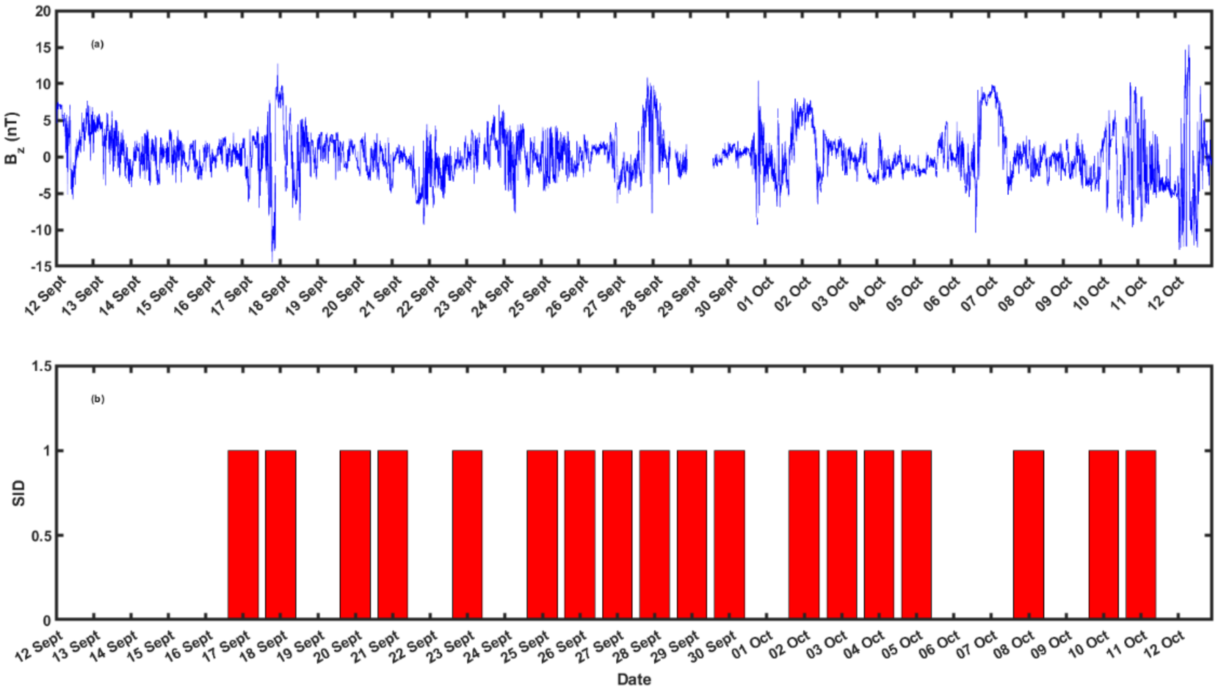

Figure 2b. Temporal variation of IMFBz (top panel) and SID events (bottom panel) during the time period 1 September 2021 - 12 October 2021.

Ap (daily average) from the World Data Center for Geomagnetism, Kyoto (http://wdc.kugi.kyoto-u.ac.jp/) accessed on 29 May, 2023 . In Figure 2(b), we present the variation of the interplanetary magnetic field (IMFBz) and Sudden Ionospheric Disturbance (SID) index during the period of 12 September to 12 October 2021. It is evident from Figure 2(a) that a minor geomagnetic storm occurred on 17 September, 2021 with Dst < –55 nT with significant enhancement of Kp (> ~4) and ap (> ~50) indices. Figure 2(b) shows the IMFBz (blue curves) and the SID events (red histograms) for the same period of time.

It is evident from Figure 2 that under the observation period, there was no such significant changes in the geomagnetic indices except the minor storm on 17 September. Also, there was some geomagnetic activity on 12 October, 2021. Thus, the possibility of contamination is minimal due to geomagnetic storms.

3.1 AGW anomalies from SABER/TIMED satellites

Figure 3 shows the altitude profile of potential energy Ep of the generated waves as computed from the perturbation temperature profiles as described in the previous section. The Ep profiles are computed from 12 September to 1 October (±15 days) around the EQ. The altitude ranges from 30 to 50 kilometres. The PE value ranges from 0 to 12 J/kg. The vertical dashed line is the day of the EQ. It is evident that an intensification of AGW energy is observed at an altitude of 42 to 47 kilometres. Based on the enhancement in Ep values, in Figure 4, we present the spatio-temporal profile of the Ep from 19/09/2021 to 27/09/2021. We choose the latitude and longitude ranges from 25° to 45° N and 15° to 25° E keeping the EQ epicenter at the centre (violet diamond). It is evident from the figure that Ep values started to increase on 22 September around the epicenter and became maximum on 24 September, 2021. As similarly to Figure 4, the Ep shows normal value on the EQ day. The intensified patch started to increase in the northern direction and migrate and dissipates towards the south-eastern direction of the EQ epicenter. We check the possibilities of thunderstorms and rainfalls that may arise the atmospheric instability and convective movements and can generates AGWs using the Ventusky search engine (https://www.ventusky.com (accessed on 24 May 2023)). We found that during the intensification period of AGW energy budget, no such activities were recorded. Thus, this intensification of AGW should have a seismic origin.

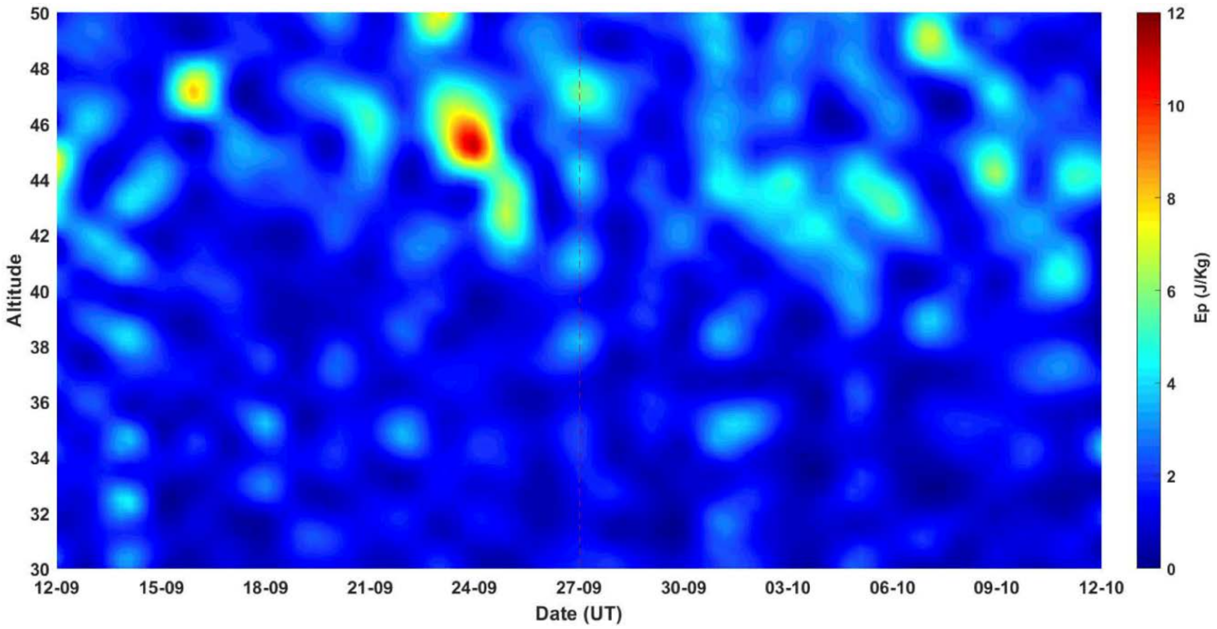

Figure 3. Altitude profile of potential energy (Ep) associated with AGWs from 12 September to 12 October, 2021. Along X and Y axes, we present the date and altitude in kilometers. The colorbar shows the Ep in J/kg. The vertical dashed line shows EQ day.

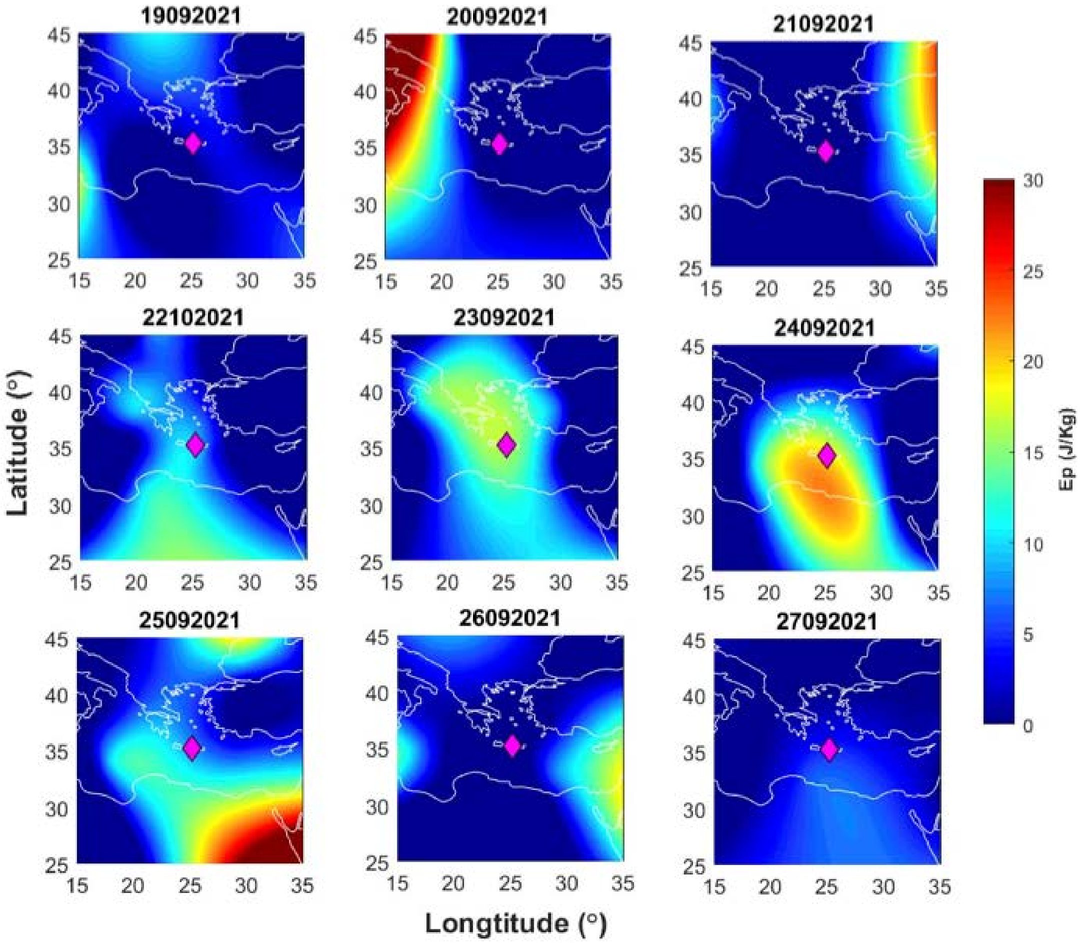

Figure 4. Spatio-temporal profile of Ep as observed at 45-kilometer altitude from 19 to 27 September, 2021. The x and y axes represent the longitude and latitude, and the colorbar shows the energy in J/kg. The violet diamond represents the EQ epicenter.

3.2 GPS-TEC Anomalies

Figure 5 illustrates the diurnal variation of the VTEC as a function of day number as computed from DYNG station (upper panel) from 12 September, 2021 to 12 October, 2021. The black curve is the observed estimated TEC and the red and green curves are the upper bound and lower bound respectively. The lower panel shows the change in the VTEC. The EQ day is marked with the downward arrow.

The diurnal profile of VTEC shows a different response in comparison to the acoustic response. The VTEC profile shows an increment above the UB on 22 September, 2021 (DOY:265). A similar enhancement with less magnitude is also observed on the day of the EQ (DOY:270) and just after the day (DOY: 271). The increase in VTEC by 4 TECU on 22 September can be possibly associated with the anomaly generated by the preparation phase of this EQ. After the day of the EQ, there are significant increases in VTEC on day numbers 275 and 276. A series of aftershocks having magnitude ranges from M = 5.3 to 4.5 took place after the main observable EQ that took place on 27 September as recorded by USGS catalogue (https://earthquake.usgs.gov). The immediate increase in VTEC on the day of the EQ and on the next day are possibly due to these events. The epicenter of the EQ on 28 September (M = 5.3) almost coincides with the mainshock. On 10 October and 12 October, a moderate (M = 5.0) and a strong (M = 6.4) EQ took place close (95 km and 64 km respectively) to the EQ epicenter of 27th September. This post-EQ VTEC enhancement can be associated as the precursory signature with these two EQs. As the magnitude of the EQ on 12 October is larger than the EQ on 27 September, the change in the VTEC value is also higher (6 TECU). As many aftershocks are recorded after 27 September, there is a possibility of an overlapping effect between the aftershocks and the next foreshocks as their preparation processes overlapped even though the Dobrolsky area covers the second EQ preparation zone and the IGS stations.

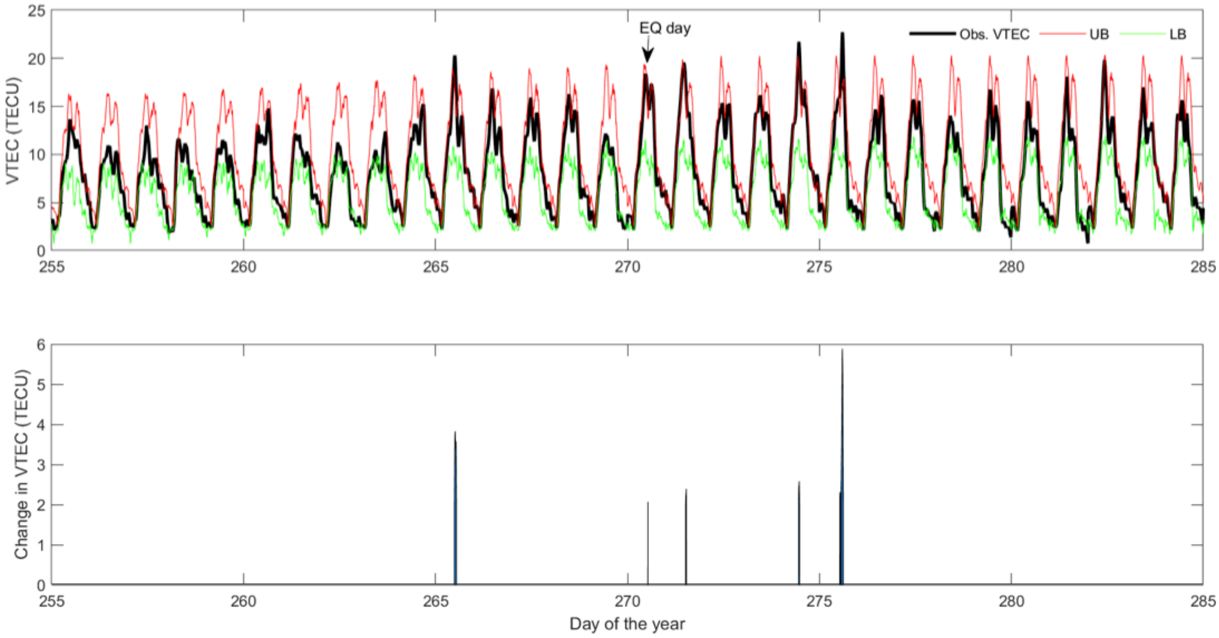

Figure 5. (Upper Panel) Diurnal variation of VTEC profiles (black curve) as a function of day number as recorded from DYNG station from 12 September, 2021 to 12 October, 2021. The red and green curves are the upper and lower bound respectively. (Lower panel) Diurnal variation as a function of day number.

3.3 AGW anomaly as computed from VTEC

To compare the SABER-TIMED observed AGW, we extract the wave-like structures as observed from the small-scale changes in the GPS-TEC profile. In the small-scale fluctuation in VTEC (dVTEC), the normal unperturbed condition can be attributed by choosing the $-0.25 \geqslant \text{dVTEC} \leq 0.25$ range. Any perturbation in small-scale fluctuations beyond this range can be considered possibly due to seismogenic origins under a quiet geomagnetic condition.

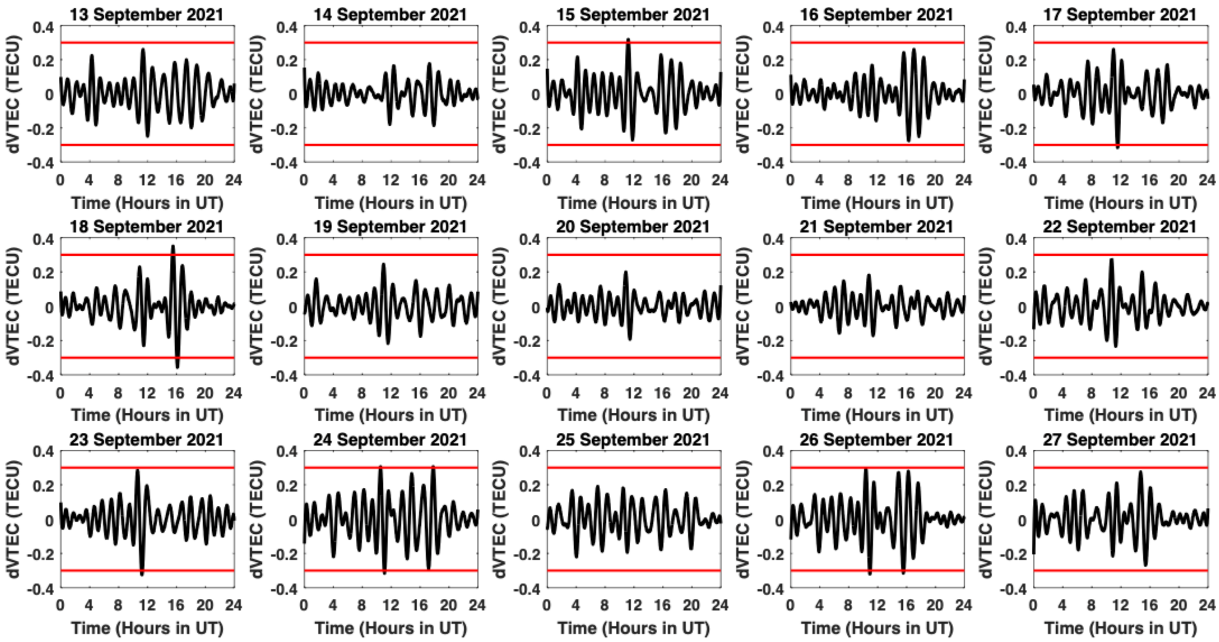

Figure 6. Diurnal variation of dVTEC (black curve) and the un-perturbed ranges (red lines) from 13 September to 27 September, 2021 for DYNG station.

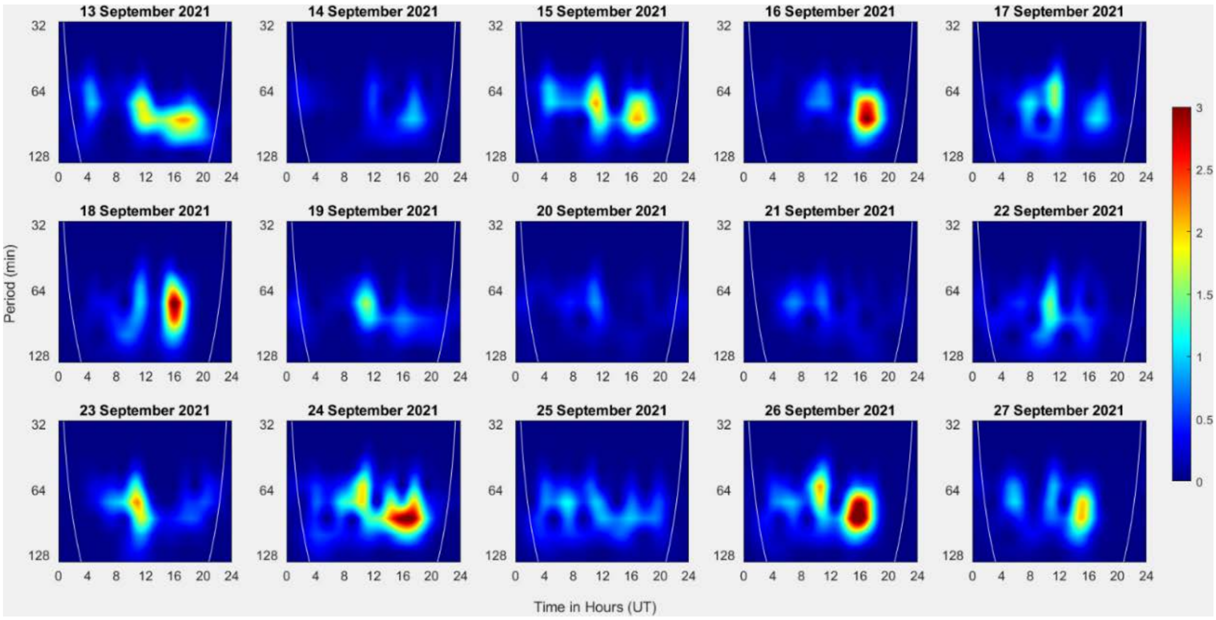

Figure 7. Scalogram contains the wavelet spectrum from 13 to 27 September, 2021 as computed from the small-scale fluctuation dVTEC for DYNG station. The x- and y-axis show the time (in hours) and wavelet period (in minutes), respectively. The colorbar shows the wavelet power. The white line represents the cone of influence (COI).

Figure 6 shows the diurnal variation of small-scale fluctuations in dVTEC (black curves) from 13-27 September 2021. The horizontal red lines indicate the unperturbed levels, as mentioned above. It is evident that the fluctuations crossed the quiet condition levels on 15, 17, 18, 23, 24, and 26 September 2021. We have mentioned in Section 2 that a geomagnetic storm occurred on 17 September 2021. So, we can ignore those days around the storm. The maximum fluctuations are found on 23, 24, and 26 September 2021. Also, as we do not observe any significant change in AGW as computed from SABER after the post-duration of the EQ, we confined ourselves to EQ Day.

To examine the wave-like structures in the dVTEC profiles, we perform a wavelet analysis, and in Figure 7, we present the wavelet power scalograms from 13 to 27 September 2021. Based on the elimination due to the effects of the geomagnetic storm, we also ignore the intensified wave energy around the storm date of 17 September. As a result, an intensified wave-like structure with a period from 90-110 minutes is found to be present on 24 September, similarly to the previous observation of AGW from SABER. Additionally, a similar identification of the period from 70-100 minutes is observed on 26 September 2021. Both intensifications lie within the AGW period, and both are found to be pre-seismic. Thus, the wavelet analysis indicates a significant presence of AGWs as computed from GPS-TEC fluctuation, corroborating with the seismogenic effects in the acoustic wave examined by other methods.

3.4 Anomalies in Particle Bursts

Figure 8 shows the diurnal variation of PBs from 12 September (DOY:255) to 12 October (DOY:285), 2021 after removing the background distribution by computing the 4σ levels as described in Section 2, where σ is the standard deviation. The black and red histograms show the PBs due to solar non-contaminated and contaminated days, respectively. Based on Figure 2(b), we marked the contaminated days according to the presence of solar activities. The dashed horizontal line represents the mean PB for the solar quiet days. The lower panel shows the non-contaminated PBs that are possible EQ associated satisfying the condition reported in Aleksandrin et al. [2003]. It is evident from Figure 8 that an enhancement of PBs is observed on the day number 257 (14 September 2021) and 267 (24 September 2021). This is interesting as the previous two parameters (VTEC, AGW) show an excellent corroboration with the anomaly on 24 September 2021. We observe another pre-seismic indication for the PB enhancement almost two weeks before the EQ. In previous findings, Chowdhury et al. [2022] reported a similar result for the Kumamoto EQ, 2016, where unusual particle (electron) burst enhancement was observed ten days before the EQ. A moderate enhancement of PBs is observed after the EQ on day number 294. This is possibly due to the strong EQ (M = 6.4) in Greece on 12 October 2021.

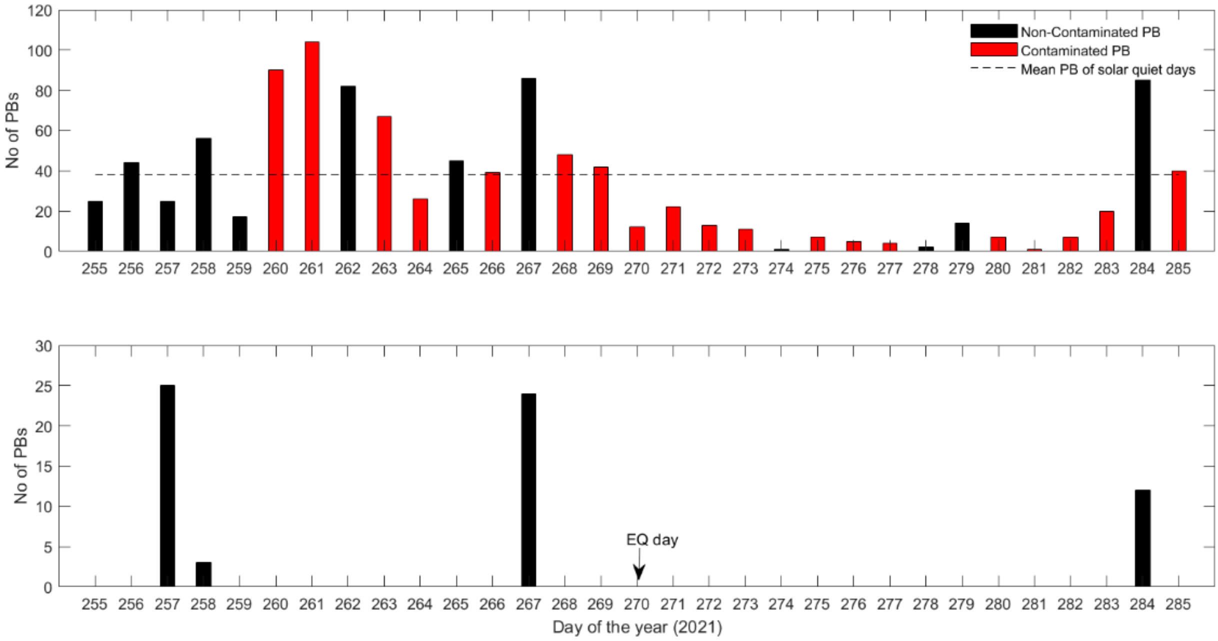

Figure 8. Diurnal variation of PBs from 12 September to 12 October, 2021. In the upper panel, the black histograms are for quite solar days, and the red histograms are contaminated due to the solar activities. The dashed horizontal line indicates the average PB. (b) The lower panel indicates the enhancement of PB 13 and 3 days before the EQ.

3.5 Anomalies in Electron Density as observed from Swarm Satellite:

We examine the electron density profiles as rapid disturbances methods for the geomagnetically and solar quiet days, as mentioned in the results in PB enhancement. We observe that the most significant anomalies occur on 24 September 2021, similarly to the other parameters. Figure 9 illustrates the outcomes of the rapid electron density disturbances as recorded on 24 September 2021. The first column shows the observed (black) and fitted (red) profiles of electron density (Ne) for the latitude from 20°N to 50° N. The middle columns show the percentage change in Ne with the mean values as denoted by red dashed lines for the latitude range from 25° to 40°N. The third column shows the satellite track (black curve) and the EQ epicenter (red star). The percentage change in Ne is high on 24 September 2021 and crossed both the upper and lower bound of the mean value with a percentage change of ~7-8%. As mentioned earlier, the geomagnetic condition was quiet on this day, and thus this anomaly could possibly be associated with the EQ.

4. Discussions

The manuscript presents the possible pre-seismic anomalies for the 2021 Crete EQ on September 27, 2021, with a magnitude M = 6.0. We use several ground- and space-based techniques covering LAIC's acoustic and thermal channels. We use GPS-TEC profiles as recorded from the DYNG ISG station for the ground-based method. We use SABER-TIMED satellite temperature profiles, NOAA radiation belt PB profiles, and Swarm satellite electron density database for the space-based study. We first start with the acoustic channel, where the AGW is computed using the temperature perturbation profile and computed from the SABER satellite. The altitude profile of potential energy of AGW (Ep) shows a significant enhancement 3 days before the EQ (24/09/2021), showing a maximum intensification at ~45-46 kilometers altitude (Figure 3). The spatio-temporal profile exhibits similar results at a 45-kilometer altitude over the epicentral region and EPZ (Figure 4). The altitude profile of Ep shows no such significant enhancement after mainshock, though there is evidence of aftershocks having magnitude M = 4.5 to 5.3.

The VTEC profile shows a significant increment 5 days before the EQ in the EM anomaly. The maximum change in the VTEC value is found to be by 4 TEC units (Figure 5). The VTEC profiles show significant enhancement after the EQ day. There was an increase in VTEC just after the EQ day possibly due to aftershocks. A much larger peak of TEC is observed during 1 and 2 October that can be associated with other strong EQs that took place on 10 and 12 October. The effect of this EQ does not exhibit in the AGW excitation in the acoustic channel of LAIC. The small-scale fluctuations in the VTEC profile (*dVTEC*) change show the prominent signature of AGW excitation in the wavelet scalograms (Figure 7). The wavelet spectrum suggests anomalous wave enhancement on 17 September due to the presence of a geomagnetic storm. However, this effect was not visible in the diurnal TEC profiles. Wave-like structures having a period of ~60 to 90 minutes are observed on 24 and 26 September 2021. The NOAA-15 satellite-based study, after eliminating SAA and possible contaminations due to SID events, shows a significant increment in PBs 3 and 13 days prior to the EQ. This is interesting as no other parameters exhibit an anomaly around 2 weeks before the EQ. The Swarm satellite electron density profiles (Ne), computed from the rapid disturbance method, show a significant percentage change in the Ne values 3 days before the EQ in the satellite track close to the EQ epicenter.

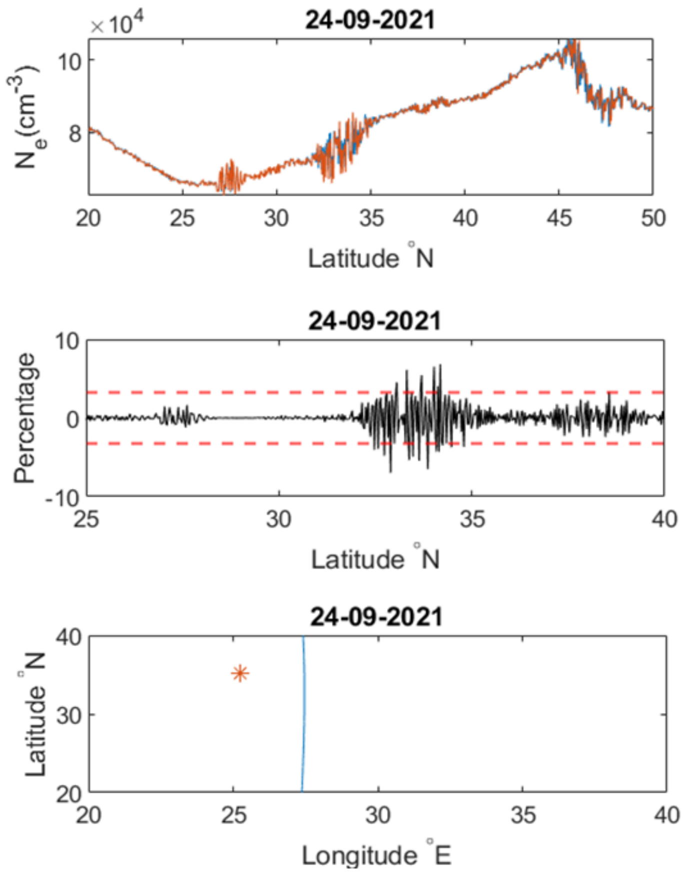

Figure 9. Electron density profile (Ne) as observed from Swarm satellite (Alpha) on 24 September, 2021. The upper column shows the observed (blue) and fitted (orange) Ne profiles for the latitude from 20°N to 50°N. The middle panel shows the percentage change in Ne along with the mean values denoted by horizontal dashed lines. The third column shows the satellite track with the EQ epicenter (red star)

During the observable period, the geomagnetic conditions were mostly quiet except for a minor geomagnetic storm on 17 September 2021. Figures 2(a, b) show the geomagnetic condition. It is evident that the pre-seismic period when all the parameters show significant anomalies, is free from contamination due to any geomagnetic and solar activities. Similarly, another geomagnetic disturbance took place on 12 October which is also far from the EQ day and thus has no such a contaminated effect. During the 2020 Samos EQ, as Sasmal et al. [2021] reported, the different parameters show different time scales of maximum anomalies before the EQ Day. However, for this Crete EQ, all the parameters show maximum intensification 3 days prior to the EQ except the PB values. Another exciting factor is the diurnal TEC anomalies, where the effect of post-EQ and aftershocks are significantly prominent. The impact of the geomagnetic storm is only visible from the small-scale fluctuations computed from the VTEC profiles. This is also reflected in the wave-like structures in the wavelet scalograms. It is evident from the multi-parametric results that Crete EQ shows less inhomogeneity in terms of the temporal evolution of the anomalous parameters. Other phenomena like thermal anomalies [Peleli et al., 2022] and sub-ionospheric VLF anomalies [Politis et al., 2023] also show significant seismogenic effects.

5. Conclusions

It is reasonable that the complex pre-seismic process involves many parameters with interrelated geochemical and geophysical origins. The fundamental concept of LAIC that involves the different channels has a prominent nature of inhomogeneity and anisotropy, leading to different temporal profiles of the maximum anomalies (See Introduction). This is reflected in the induvial studies where different parameters show different anomaly signatures. Therefore, the multi-parametric approach can give a comprehensive idea about the importance of various parameters for a single EQ and their interrelationship (if any). The 2021 Crete EQ arose the opportunity for such a study where we analyze the acoustic and EM anomalies recorded from ground- and space-based observables. The outcomes of this analysis from GPS-TEC, AGW, PB enhancement, TEC-associated AGW, and Swarm electron density show convincing pre-seismic impression and, most interestingly, on the same day (24 September 2021) before the EQ under a quiet geomagnetic condition. Interestingly, even though the magnitude of the EQ is moderate (M = 6), the anomalous signature is quite prominent in most parameters. Another EQ that took place on 12 October having a larger magnitude (M = 6.5), can create some pre-seismic effects during its preparation process. The pre-seismic effects and their physical propagation mechanism are widely debated as not adequately understood. Also, how the anomalies of different channels migrate from one atmospheric layer to another is a highly complicated phenomenon regarding their source and characteristics. Therefore, even though case studies of the multi-parametric approach give convincing outcomes of seismogenic effects, statistical analysis is necessary to identify the most significant and useful parameters of the LAIC mechanism. This will be done in the future.

Acknowledgment. The authors acknowledge all the database sources for providing the data for analysis.

References

Anagnostopoulos, G., E. Vassiliadis and S. Pulinets (2012). Characteristics of flux-time profiles, temporal evolution, and spatial distribution of radiation-belt electron precipitation bursts in the upper ionosphere before great and giant earthquakes. Ann. Geophys., 55, 21-36.

Balasis, G. and M. Mandea (2007). Can electromagnetic disturbances related to the recent great earthquakes be detected by satellite magnetometers?, Tectonophysics, 431, 173-195.

Battiston, R. and V. Vitale (2013). First evidence for correlations between electron fluxes measured by NOAA-POES satellites and large seismic events, Nucl. Phys. Proc. Suppl., 243, 249-257.

Biswas, S., S. Kundu, S. Ghosh, S. Chowdhury, S.-S. Yang, M. Hayakawa, S. Chakraborty, S.K. Chakrabarti and S. Sasmal (2020). Contaminated effect of geomagnetic storms on pre-seismic atmospheric and ionospheric anomalies during Imphal earthquake, Open J. Earthq. Res, 09, 383-402.

Biswas, S., S. Chowdhury, S. Sasmal, D.Z. Politis, S.M. Potirakis and M. Hayakawa (2022). Numerical modelling of sub-ionospheric very low frequency radio signal anomalies during the Samos (Greece) earthquake (M = 6.9) on October 30, 2020, Adv. Space Res., 70, 5, 1453-1471.

Biswas, S., S. Kundu, S. Sasmal, D.Z. Politis, S.M. Potirakis and M. Hayakawa (2023). Preseismic perturbations and their inhomogeneity as computed from ground- and space-based investigation during the 2016 Fukushima earthquake, J. Sensors, 7159204.

Chakrabarti, S.K., M. Saha, R. Khan, S. Mandal, K. Acharyya and R. Saha (2005). Possible detection of ionospheric disturbances during the Sumatra-Andaman islands earthquakes of December, 2004, Indian J. Radio Space Phys., 34, 314-317.

Chakrabarti, S., S. Sasmal, M. Saha, R. Khan, D. Bhoumik and S.K. Chakrabarti (2007). Unusual behavior of D-region ionization time at 18.2kHz during seismically active days, Indian J. Phys., 81, 5, 531-538.

Chakrabarti, S.K., S. Sasmal and S. Chakrabarti (2010). Ionospheric anomaly due to seismic activities — Part 2: Evidence from D-Layer preparation and disappearance times, Nat. Haz. Earth Syst. Sci., 10, 1751-1757.

Chakraborty, S., S. Sasmal, T. Basak, S. Ghosh, S. Palit, S.K. Chakrabarti and S. Ray (2017). Numerical modeling of possible lower ionospheric anomalies associated with Nepal earthquake in May, 2015, Adv. Space Res., 60, 8, 1787-1796.

Chakraborty, S., S. Sasmal, S.K. Chakrabarti and A. Bhattacharya (2018). Observational signatures of unusual outgoing longwave radiation (OLR) and Atmospheric Gravity Waves (AGW) as precursory effects of May 2015 Nepal earthquakes, J. Geodyn., 113, 43-51.

Chowdhury, S., S. Kundu, S. Ghosh, M. Hayakawa, A. Schekotov, S.M. Potirakis, S.K. Chakrabarti and S. Sasmal (2022). Direct and indirect evidence of pre-seismic electromagnetic emissions associated with two large earthquakes in Japan, Nat Hazards, 112, 2403-2432.

Chen, H., P. Han and K. Hattori (2022). Recent Advances and Challenges in the Seismo- Electromagnetic Study: A Brief Review, Remote Sens., 14, 5893.

Chetia, T., G. Sharma, C. Dey and P.L.N. Raju (2020). Multi-Parametric Approach for Earthquake Precursor Detection in Assam Valley (Eastern Himalaya, India) using Satellite and Ground Observation Data, Geotecton, 54, 83-96.

Clilverd, M.A., C.J. Rodger and N.R. Thomson (1999). Investigating seismoionospheric effects on a long subionospheric path, J. Geophys. Res., 104, 28171-28179

Dobrovolsky, I.R., S.I. Zubkov and V.I. Myachkin (1979). Estimation of the size of earthquake preparation zones. Pure Appl. Geophys. 117, 1025-1044.

De Santis, A., G. De Franceschi, L. Spogli and L. Perrone, et al. (2015). Geospace perturbations induced by the Earth: The state of the art and future trends, Phys. Chem. Earth, Parts A/B/C, 85-86, 17-33.

De Santis, A., D. Marchetti and L. Spogli, et al. (2019). Magnetic Field and Electron Density Data Analysis from Swarm Satellites Searching for Ionospheric Effects by Great Earthquakes: 12 Case Studies from 2014 to 2016, Atmosphere, 10, 371.

De Santis, A., D. Marchetti and F.J. Pavón-Carrasco, et al. (2019). Precursory worldwide signatures of earthquake occurrences on Swarm satellite data, Sci. Rep., 9, 20287.

De Santis, A., D. Marchetti, L. Spogli and G. Cianchini, et al. (2019). Magnetic Field and Electron Density Data Analysis from Swarm Satellites Searching for Ionospheric Effects by Great Earthquakes: 12 Case Studies from 2014 to 2016, Atmosphere, 10, 7, 371

Garner, T., T. Gaussiran, B.W. Tolman, R.B. Harris, R.S. Calfas and H. Gallagher (2008). Total electron content measurements in ionospheric physic, Adv. Space Res., 42, 720-726.

Fetzer, E.J. and J.C. Gille (1994). Gravity wave variation in LIMS temperatures. Part I: Variability and comparison with background winds, J. Atmos. Sci., 51, 2461-2483.

Fidani, C. and R. Battiston (2008). Analysis of NOAA particle data and correlations to seismic activity. Nat. Hazards Earth Syst. Sci., 8, 1277-1291.

Fidani, C. (2021). West Pacific Earthquake Forecasting Using NOAA Electron Bursts with Independent L-Shells and Ground-Based Magnetic Correlations, Front. Earth Sci., 9, 673105.

Fidani, C. (2022). The Conditional Probability of Correlating East Pacific Earthquakes with NOAA Electron Bursts, Appl. Sci., 12, 1052.

Gorny, V.I., A.G. Salman, A.A. Tronin and B.V. Shilin (1998). The Earth's outgoing IR radiation as an indicator 458 of seismic activity, Proc. Acad. Sci. USSR, 301, 67-69.

Ghosh, S., S. Chakraborty, S. Sasmal, T. Basak, S.K. Chakrabarti and A. Samanta (2019). Comparative study of the possible lower ionospheric anomalies in very low frequency (VLF) signal during Honshu, 2011 and Nepal, 2015 earthquakes, Geomat. Nat. Hazards Risk, 10, 1596-1612.

Ghosh, S., S. Chowdhury, S. Kundu, S. Sasmal, D.Z. Politis, S.M. Potirakis, M. Hayakawa, S. Chakraborty and S.K. Chakrabarti (2021). Unusual surface latent heat flux variations and their critical dynamics revealed before strong earthquakes, Entropy, 24, 1, 23.

Ghosh, S., S. Sasmal, M. Naja, S. Potirakis and M. Hayakawa (2023). Study of aerosol anomaly associated with large earthquakes, Adv. Space Res., 71, 1, 129-143.

Ghosh, S., S. Sasmal, S. Midya, S.K. Chakrabarti (2017). Unusual Change in Critical Frequency of F2 Layer during and 447 Prior to Earthquakes, Open J. Earthq. Res. , OJER, 6, 191-203.

Korepanov, V., M. Hayakawa, Y. Yampolski and G. Lizunov (2009). AGW as a seismo-ionospheric coupling responsible agent, Phys. Chem. Earth Parts A/B/C 2009, 34, 485-495.

He, Y., X. Zhao, D. Yang, Y. Wu and Q. Li (2022). A study to investigate the relationship between ionospheric disturbance and seismic activity based on Swarm satellite data, Phys. Earth Planet. Int., 23, 106826.

Hayakawa, M., O.A. Molchanov, T. Ondoh and E. Kawai (1996a). The Precursory Signature Effect of the Kobe Earthquake on VLF Sub-Ionospheric Signals, J. Comm. Res. Lab., 43, 2, 169-180.

Hayakawa, M., O.A. Molchanov, T. Ondoh and E. Kawai (1996b). Anomalies in the sub-ionospheric VLF signals for the 1995 Hyogo-Ken Nanbu earthquake, J. Phys. Earth, 44, 4, 413-418.

Hayakawa, M. (2007). VLF/LF Radio Sounding of Ionospheric Perturbations Associated with Earthquakes, Sensors, 7, 1141-1158.

Hayakawa, M., J. Izutsu, A. Schekotov, S.S. Yang, M. Solovieva and E. Budilova (2021). Lithosphere-atmosphere-ionosphere coupling effects based on multiparameter precursor observations for February-March 2021 earthquakes (M~7) in the offshore of Tohoku area of Japan, Geosci., 11, 11, 481.

Hayakawa, M., A. Schekotov, S. Izutsu, S.S. Yang, M. Solovieva and Y. Hobara (2022). Multi-parameter observations of seismogenic phenomena related to the Tokyo earthquake (M = 5.9) on 7 October 2021, Geosci., 12, 7, 265.

Hayakawa M., A. Schekotov, J. Izutsu, A.P. Nickolaenko (2019). Seismogenic effects in ULF/ELF/VLF electromagnetic waves, Int. J. Electron. Appl. Res., 6, 2, 1-86.

Hayakawa, M., A. Schekotov, J. Izutsu, A.P. Nickolaenko and Y. Hobara (2023). Seismogenic ULF/ELF Wave Phenomena: Recent Advances and Future Perspectives, Open J. Earthq. Res., 12, 45-113.

Liu, J.Y., C.H. Chen, C.H. Lin, H.F. Tsai, C.H. Chen and M. Kamogawa (2011). Ionospheric disturbances triggered by the 11 March 2011 M9.0 Tohoku earthquake, J. Geophys. Res.: Space Phys., 116, A06319.

Liu, J.Y, Y.I. Chen, Y.J. Chuo and H.F. Tsai (2001). Variations of ionospheric total electron content during the Chi-Chi Earthquake, Geophys. Res. Lett., 28, 1383-1386

Liu, J.Y, Y.J. Chuo, S.J. Shan, Y.B. Tsai, Y.I. Chen, S.A. Pulinets and S.B. Yu (2004). Pre-earthquake ionospheric anomalies registered by continuous GPS TEC measurements, Ann. Geophysicae, 22, 1585-1593.

Liu, D. (2000). Anomalies analyses on satellite remote sensing OLR before Jiji earthquake of Taiwan Province, Geo Info. Sci., 2, 1, 33-36.

Kundu, S., S. Chowdhury, S. Ghosh, S. Sasmal, D.Z. Politis, S.M. Potirakis, S.S. Yang, S.K. Chakrabarti and M. Hayakawa (2022). Seismogenic Anomalies in Atmospheric Gravity Waves as Observed from SABER/TIMED Satellite During Large Earthquakes, J. Sensors, Article ID 3201104, 23.

Marchetti, D., A. De Santis, S. D'Arcangelo, F. Poggio, A. Piscini, S.A. Campuzano and W.V.J.O. de Carvalho (2019). Pre-Earthquake Chain Processes Detected from Ground to Satellite Altitude in Preparation of the 2016-2017 Seismic Sequence in Central Italy, Remote Sens. Environ., 229, 93-99.

Marchetti, D., A. De Santis, S.A. Campuzano, K. Zhu, M. Soldani, S. D'Arcangelo, M. Orlando, T. Wang, G. Cianchini and D. Di Mauro, et al. (2022). Worldwide Statistical Correlation of Eight Years of Swarm Satellite Data with M5.5+ Earthquakes: New Hints about the Preseismic Phenomena from Space, Remote Sens., 14, 2649.

Maurya, A.K., K. Venkatesham, P. Tiwari, K. Vijaykumar, R. Singh, A.K. Singh and D.S. Ramesh (2016). The 25 April 2015 Nepal earthquake: Investigation of Precursor in VLF Subionospheric Signal, J. Geophys. Res.: Space Phys., 121, 10.

Molchanov, O.A. and M. Hayakawa (1995). Generation of ULF electromagnetic emissions by microfracturing, Geophys. Res. Lett., 22, 22, 3091-3094.

Molchanov, O.A., O.A. Mazhaeva, A.N. Golyavin and M. Hayakawa (1993). Observation by the Intercosmos-24 satellite of ELF-VLF electromagnetic emissions associated with earthquakes, Ann. Geophysicae, 11, 431-440.

Nina, A., P.F. Biagi, S.T. Mitrović, S. Pulinets, G. Nico, M. Radovanović and L.Č. Popović (2021). Reduction of the VLF signal phase noise before earthquakes, Atmosphere, 12, 4, 444.

Omori, Y., Y. Yasuoka, H. Nagahama, Y. Kawada, T. Ishikawa, S. Tokonami and M. Shinogi (2007). Anomalous radon emanation linked to preseismic electromagnetic phenomena, Nat. Hazards Earth Syst. Sci., 7, 629-635, https://doi.org/10.5194/nhess-7-629-2007

Ouzounov, D., S. Pulinets, D. Davidenko, A. Rozhnoi, M. Solovieva, V. Fedun, B.N. Dwivedi, A. Rybin, M. Kafatos and P. Taylor (2021). Transient Effects in Atmosphere and Ionosphere Preceding the 2015 M7.8 and M7.3 Gorkha-Nepal Earthquakes, Front. Earth Sci., 9, 757358.

Pal, P., S. Sasmal and S.K. Chakrabarti (2017). Studies of seismo-ionospheric correlations using anomalies in phase of very low frequency signal, Geomat. Nat. Haz. Risk, 8, 167-176.

Peleli, S., M. Kouli and F. Vallianatos (2022). Satellite-Observed Thermal Anomalies and Deformation Patterns Associated to the 2021, Central Crete Seismic Sequence. Remote Sens., 14, 3413.

Piersanti, M., M. Materassi, R. Battiston, V. Carbone, A. Cicone, G. D'Angelo, P. Diego and P. Ubertini (2020). Magnetospheric-ionospheric-lithospheric coupling model. 1: Observations during the 5 August 2018 Bayan earthquake, Remote Sens., 12, 20, 3299.

Politis, D.Z., S.M. Potirakis, Y.F. Contoyiannis, S. Biswas, S. Sasmal and M. Hayakawa (2021). Statistical and criticality analysis of the lower ionosphere prior to the 30 October 2020 Samos (Greece) earthquake (M6.9), based on VLF electromagnetic propagation data as recorded by a new VLF/LF receiver installed in Athens (Greece), Entropy, 23(6), 676.

Politis, D.Z., S.M. Potirakis, S. Kundu, S. Chowdhury, S. Sasmal and M. Hayakawa (2022). Critical dynamics in stratospheric potential energy variations prior to significant (M > 6.7) earthquakes, Symmetry, 14, 1939.

Popov K.V., V.A. Liperovsky, C.V. Meister, P.F. Biagi, E.V. Liperovskaya and A.S. Silina (2004). On ionospheric precursors of earthquakes in scales of 2-3 h, Phys. Chem. Earth, 29, 4-9, 529-535.

Potirakis, S.M., K. Eftaxias, A. Schekotov, H. Yamaguchi and M. Hayakawa (2016). Criticality features in ultra-low frequency magnetic fields prior to the 2013 M6.3 Kobe earthquake, Ann. Geophysics, 59, 3, S0317.

Potirakis, S.M., T. Asano and M. Hayakawa (2018). Criticality analysis of the lower ionosphere perturbations prior to the 2016 Kumamoto (Japan) earthquakes as based on VLF electromagnetic wave propagation data observed at multiple stations, Entropy, 20, 3, 199.

Pulinets, S.A. and D. Ouzounov (2011). Lithosphere-Atmosphere-Ionosphere coupling (LAIC) model—An unified concept for earthquake precursors validation, J. Asian Earth Sci., 2011, 41, 371-382.

Pulinets, S. and K. Boyarchuk (2004). Ionospheric Precursors of Earthquakes, Springer, Berlin.

Ray, S., S.K. Chakrabarti, S. Sasmal, A.K. Choudhury and S.K. Chakrabarti (2010). Correlations between the anomalous behaviour of the ionosphere and the seismic events for VTX-MALDA VLF propagation, AIP Conf. Proc., 1286, 298.

Ray, S., S.K. Chakrabarti, S.K. Mondal and S. Sasmal (2011). Ionospheric anomaly due to seismic activities-III: Correlation between night time VLF amplitude fluctuations and effective magnitudes of earthquakes in Indian sub-continent, Nat. Hazards Earth Syst. Sci., 11, 2699-2704.

Ray, S., S.K. Chakrabarti and S. Sasmal (2012). Precursory effects in the nighttime VLF signal amplitude for the 18th January, 2011 Pakistan earthquake, Indian J. Phys., 86, 85-88.

Remsberg, E.E., B.T. Marshall, M. Garcia-Comas, D. Krueger, G.S. Lingenfelser, J. Martin-Torres, M.G. Mlynczak, J.M. Russell, A.K. Smith and Y. Zhao (2008). Assessment of the quality of the version 1.07 temperature-versus--pressure profiles of the middle atmosphere from TIMED/SABER, J. Geophys. Res., 2008, 113, D17101.

Rozhnoi, A., M. Solovieva and M. Hayakawa (2013). VLF/LF signals method for searching of electromagnetic earthquake precursors, Earthquake prediction studies: Seismo electromagnetics, M Hayakawa (Editor), Tokyo, Japan, 31-48.

Rozhnoi, A., M. Hayakawa, M. Solovieva, Y. Hobara and V. Fedun (2014). Ionospheric effects of the Mt. Kirishima volcanic eruption as seen from Subionospheric VLF Observations, J. Atmos. Sol.-Terr. Phys., 107, 54-59.

Sasmal, S. and S.K. Chakrabarti (2009). Ionospheric anomaly due to seismic activities – Part 1: Calibration of the VLF signal of VTX 18.2 kHz station from Kolkata and deviation during seismic events, Nat. Hazards Earth Syst. Sci., 9, 1403-1408.

Sasmal, S., S.K. Chakrabarti and S. Chakrabarti (2010). Studies of the correlation between ionospheric anomalies and seismic activities in the Indian subcontinent, Conference Proceedings of Propagation Effects of Very Low Frequency Radio Waves, Edited by S.K. Chakrabarti, AIP Conf. Proc., 1286, 362.

Sasmal, S., S.K. Chakrabarti and S. Ray (2014). Unusual behavior of very low frequency signal during the earthquake at Honshu/Japan on 11 March, 2011, Indian J. Phys, 88, 1013-1019.

Sasmal, S., S. Chowdhury, S. Kundu, D.Z. Politis, S.M. Potirakis, G. Balasis, M. Hayakawa and S.K. Chakrabarti (2021). Pre-seismic irregularities during the 2020 Samos (Greece) earthquake (M = 6.9) as investigated from multi-parameter approach by ground and space-based techniques, Atmosphere, 12, 8, 1059.

Seemala, G.K. and C.E. Valladares (2011). Statistics of total electron content depletion observed over the South American continent for the year 2008, Radio Sci., 46, RS5019.

Schekotov, A., O. Molchanov, K. Hattori, E. Fedorov, V.A. Gladyshev, G.G. Belyaev, V. Chebrov, V. Sinitsin, E. Gordeev and M. Hayakawa (2006). Seismo-ionospheric depression of the ULF geomagnetic fluctuations at Kamchatka and Japan, Phys. Chem. Earth, 31, 313-318.

Shalimov, S.L. (1992). Lithosphere-ionosphere relationship: A new way to predict earthquakes?, Intern. Geosci. Newsmag., 15, 252-254.

Thurairajah, B., S.M. Bailey, C.Y. Cullens, M.E. Hervig and J.M. Russell (2014). Gravity wave activity during recent stratospheric sudden warming events from SOFIE temperature measurements, J. Geophys. Res.: Atmos., 119, 8091-8103.

Wu, L., Y. Qi, W. Mao, J. Lu, Y. Ding, B. Peng and B. Xie (2023). Scrutinizing and Rooting the Multiple Anomalies of Nepal Earthquake Sequence in 2015 with the Deviation-Time-Space Criterion and Homologous Lithosphere-Coversphere-Atmosphere-Ionosphere Coupling, Physics. Nat. Hazards Earth Syst. Sci., 23, 231-249.

Yang, S.S., S.M. Potirakis, S. Sasmal and M. Hayakawa (2020). Natural Time Analysis of global navigation satellite system surface deformation: The case of the 2016 Kumamoto earthquakes, Entropy, 22, 6, 674.

Yoshida, M., T. Yamauchi, T. Horie and M. Hayakawa (2008). On the generation mechanism of terminator times in sub-ionospheric VLF/LF propagation and its possible application to seismogenic effects, Nat. Hazards Earth Syst., 8, 129-134.

Zhang, Y., T. Wang, W. Chen, K. Zhu, D. Marchetti, Y. Cheng, M. Fan, S. Wang, J. Wen and D. Zhang, et al. (2023). Are There One or More Geophysical Coupling Mechanisms before Earthquakes? The Case Study of Lushan (China) 2013, Remote Sens., 15, 1521.

***CORRESPONDING AUTOR: Sudipta SASMAL**,
Institute of Astronomy Space and Earth Science, Kolkata, India
e-mail: sudipta@iases.org.in